




Cite this: *Mater. Adv.*, 2023,  
4, 2636

Received 15th March 2023,  
Accepted 16th May 2023

DOI: 10.1039/d3ma00123g

rsc.li/materials-advances

# Efficiently improving the adsorption capacity of the Rhodamine B dye in a SO<sub>3</sub>H-functionalized chromium-based metal–organic framework†

Khang M. V. Nguyen, Anh V. N. Phan, Nhung T. Dang, Truong Q. Tran,  
Huy K. Duong, Hung N. Nguyen and My V. Nguyen \*

A metal–organic framework containing metal sites of chromium, termed BUT-8(Cr), was successfully fabricated via a solvothermal procedure, which is capable of excellent uptake of the Rhodamine B (RhB) dye from the solution. The removal of the RhB dye using BUT-8(Cr) was studied in terms of solution pH, material content, adsorption isotherms, and kinetics to identify the most favorable conditions. Accordingly, the maximum adsorption capacity of 811.7 mg g<sup>−1</sup> is well-fitted by the Langmuir isotherm model, which is much higher than those of previously reported MOF materials. Furthermore, the kinetic data for the RhB adsorption fit with the pseudo-second order model. This indicates that RhB uptake is a chemical process. The recycling test result shows that an efficiency of 94.5% is retained over seven recycles. The comparison of the results of FT-IR and Raman spectroscopy, and PXRD, and TGA-DSC analyses of RhB⊂BUT-8(Cr) reveals the presence of electrostatic and  $\pi$ – $\pi$  interactions between the RhB<sup>+</sup> ions and negatively charged SO<sub>3</sub><sup>−</sup> moieties within the MOF architecture, leading to RhB removal with an ultra-high adsorption capacity. These findings show that the sulfonic-functionalized Cr-based MOF could be a promising candidate for removing organic dyes in a real polluted environment.

## 1. Introduction

To date, various treatment techniques have been developed to find solutions for organic dye elimination in wastewater. These dyes are popular colorants used in textile, paint, cosmetics, leather, visualizing microplastics, and related industries,<sup>1–3</sup> released directly into the natural water environment. Rhodamine B (RhB) is a toxic cationic dye of the xanthene class. The presence of RhB in water sources brings negative effects on human health and ecosystems. Particularly, it causes skin and eye irritation, neurotoxicity, and serious problems to the photo-synthetic process of aquatic plants and is a cancer-causing agent.<sup>4–8</sup> Herein, the aromatic rings in the structure of RhB make it more stable and harder to be biologically oxidated or eliminated photocatalytically.<sup>9</sup> Hence, dye-effluent treatment techniques and their developments turn out to be research challenges. Generally, the removal of organic dyes can be performed using various methods, including precipitation–deposition, electrocoagulation, membrane filtration, advanced oxidation, and electrochemical techniques.<sup>10–19</sup> Apart from the

stated procedures, adsorption is considered the most effective treatment method because of its economic feasibility, easy operation, simplicity, and high efficiency.<sup>20–23</sup> Recently, adsorbents have been utilized to separate organic dyes from wastewater, such as activated carbon,<sup>24</sup> fibers,<sup>25</sup> metal oxides,<sup>26</sup> biosorbents,<sup>27–29</sup> clay,<sup>30</sup> graphene oxide,<sup>31</sup> and zeolites.<sup>32</sup> However, these materials still have disadvantages in the adsorption applications due to their low capacity, slow kinetics, complex processes, and being economically unattractive in some cases. Therefore, preparing and employing alternative adsorbents for organic dye elimination from wastewater is highly desirable. Among the recently discovered adsorbents, metal–organic frameworks (MOFs) are known for their porous morphology with adjustable pore size and modification of functional groups on the ligand, resulting in remarkable advantages such as large surface area, low density, and high thermal and chemical stability.<sup>33–38</sup> Interestingly, the MOF structure can be controlled, allowing the generation of effective interactions between guest molecules and the adsorption sites, opening unique applications related to adsorption.<sup>39–44</sup> Noteworthy, chromium-based MOFs have emerged as ultra-high water stable materials because of their robust metal–carboxylate bonds and rigid frameworks, leading to many applications of adsorption under practical conditions.<sup>45,46</sup>

Faculty of Chemistry, Ho Chi Minh City University of Education, Ho Chi Minh City, 700000, Vietnam. E-mail: mynv@hcmue.edu.vn

† Electronic supplementary information (ESI) available. See DOI: <https://doi.org/10.1039/d3ma00123g>



It should be noted that the molecular size of RhB exhibits unsimilarity with the pore size of traditional absorbents and a lack of strong attraction with the adsorption sites of the materials, resulting in a low adsorption efficiency of RhB.<sup>47,48</sup> Thus, it is necessary to incorporate negatively charged adsorption sites and achieve appropriate pore sizes within MOFs for significantly enhancing the adsorption capacity of the cationic RhB ions through efficient interactions. In addition, we reported a series of Zr-based MOFs containing densely packed  $\text{SO}_3^-$  groups within the framework with an excellent adsorption capacity of  $\text{Pb}^{2+}$  and the cationic methylene blue dye *via* the effective electrostatic interaction between the positively charged moieties and anionic sulfonic sites.<sup>40,41</sup> Nevertheless, these materials possess an unsuitable pore size compared to the size of RhB molecules, leading to an insufficient adsorption capacity of RhB (*ca.* 42 mg g<sup>-1</sup>). With this in mind, we expect that the BUT-8(Cr) material with high water stability, appropriate pore size and effective electrostatic interaction between the guest molecules and the functional groups can be a potential candidate for achieving high efficiency in RhB removal from wastewater. This is a new approach to overcome the mentioned obstacles of the adsorption uptake using the previously established adsorbents.

In this study, we perform a research study using a sulfonic-functionalized Cr-based MOF, denoted as BUT-8(Cr), to effectively uptake the RhB dye *via* the electrostatic attraction between the positively charged RhB ions and the negatively charged  $\text{SO}_3^-$  moieties. As a consequence, BUT-8(Cr) showed a maximum experimental adsorption capacity of 811.7 mg g<sup>-1</sup> for RhB at pH = 3 and could be recycled at least seven times. Remarkably, the structural characteristics and adsorption mechanism of RhB onto BUT-8(Cr) were interpreted *via* the adsorption models combined with the methods such as Fourier transform infrared (FT-IR) spectroscopy, Raman spectroscopy, powder X-ray diffraction (PXRD), and thermogravimetric analysis (TGA). These obtained data demonstrate that the BUT-8(Cr) material has potential applications as an effective absorbent to capture RhB dyes from an aqueous medium.

## 2. Experimental section

### Materials and general procedures

All the utilized chemicals, including 2,6-naphthalenedicarboxylic acid ( $\text{H}_2\text{NDC}$ , 98%), chromium nitrate ( $\text{Cr}(\text{NO}_3)_3 \cdot 9\text{H}_2\text{O}$ , 98%), oleum ( $\text{SO}_3$  in concentrated  $\text{H}_2\text{SO}_4$ , 20%), *N,N*-dimethylformamide (DMF, 98%), hydrochloric acid (HCl, 37%), hydrofluoric acid (HF, 47%), and methanol (MeOH, 99%) were purchased from commercially available sources and used without further purification. Herein, the 4,8-disulfonaphthalene-2,6-dicarboxylic acid ( $\text{H}_4\text{SNDC}$ ) linker and MIL-101-NDC were prepared according to the previously reported works.<sup>40,41,49,50</sup>

Raman spectroscopy analysis was performed on a spectrometer (XploRA one 532 nm, Horiba). Fourier transform infrared (FT-IR) spectra were obtained on a spectrometer with the Attenuated Total Reflectance sampling method (FT/IR-6600,

Jasco). Powder X-ray diffraction data were obtained on a diffractometer (D8 Advance, Bruker) using a Ni filtered Cu K $\alpha$  source ( $\lambda = 1.54718 \text{ \AA}$ ). The  $2\theta$  range was 3–50° with a step size of 0.02° and a fixed counting time of 0.5 s/step. Thermogravimetric analysis (TGA) and differential scanning calorimetry (DSC) diagrams were obtained on a thermal analysis system (Labsys Evo 1600 TGA, SETARAM) under dry airflow and in the temperature range of 25–800 °C at a rate of 10 °C min<sup>-1</sup>. Solution <sup>1</sup>H-NMR spectra were analyzed on an NMR spectrometer (AVANCE Neo 600 MHz, Bruker). Accordingly,  $\text{H}^+ \subset \text{BUT-8}(\text{Cr})$  was digested in  $\text{DMSO-d}_6$  solution containing 10  $\mu\text{L}$  of HF. Then, the mixture was sonicated for 10 minutes before <sup>1</sup>H-NMR measurement. Low pressure  $\text{N}_2$  adsorption analyses were performed on a surface characterization analyzer (3Flex, Micromeritics). Helium was used for the estimation of dead space. A liquid  $\text{N}_2$  bath was employed for measurements at 77 K. Before  $\text{N}_2$  sorption measurements, the material was activated at 80 °C under vacuum ( $10^{-2}$  kPa) for 48 h. Scanning electron microscopy (SEM) images were acquired utilizing a microscope (FESEM S-4800, Hitachi) with an accelerating voltage of 10 kV connected to energy-dispersive X-ray (EDX) mapping analyzed on an instrument (EDX H-7593, Horiba). Transmission electron microscopy (TEM) was carried out using a microscope (Jeon 1010, Hitachi) with a high voltage of 80 kV. UV-Vis spectra were obtained on a spectrometer (Lambda 25, PerkinElmer). Notably, the surface area was determined using *Materials Studio 7.0* software with a grid interval of 0.25 Å and a solvent diameter of 3.68 Å. The accessible solvent surface for a unit cell was indicated in the analysis tab and used for counting the value of surface area per gram (Table S1 and Fig. S10, ESI†).

### Synthesis of $\text{DMA} \subset \text{BUT-8}(\text{Cr})$

According to the previously reported work,<sup>49</sup> a mixture of  $\text{Cr}(\text{NO}_3)_3 \cdot 9\text{H}_2\text{O}$  (0.400 g, 1 mmol) and  $\text{H}_4\text{SNDC}$  (0.376 g; 1 mmol) was dissolved in a 20 mL vial containing 6 mL of DMF solvent. The mixture was then transferred into a 20 mL Teflon-lined stainless-steel autoclave and 110  $\mu\text{L}$  hydrofluoric acid was added. The autoclave was heated at 190 °C for 24 h, and then slowly cooled to room temperature. Subsequently, the obtained solid was washed with the DMF solvent and then continuously soaked in hot DMF (80 mL) and deionized water (200 mL) for 24 h, respectively. After washing three times with distilled water, the mixture was immersed in MeOH for 24 h (10 mL per 4 h). Finally, the sample was collected by centrifugation and dried under dynamic vacuum at 80 °C for 24 h to yield a pure material, termed pristine BUT-8(Cr) ( $\text{DMA} \subset \text{BUT-8}(\text{Cr})$ ,  $\text{DMA} = \text{dimethylammonium}$ ) (88% yield, based on  $\text{Cr}^{3+}$ ). FT-IR ( $\text{cm}^{-1}$ , ATR): 3404 (w), 3073 (w), 2794 (w), 2461 (w), 1701 (w), 1608 (m), 1464 (w), 1412 (s), 1362 (s), 1213 (w), 1171 (s), 1032 (s), 791 (w), 768 (m), 628 (w).

### Synthesis of $\text{H}^+ \subset \text{BUT-8}(\text{Cr})$

The activated  $\text{DMA} \subset \text{BUT-8}(\text{Cr})$  was further soaked in 100 mL of a sulfuric acid solution (0.3 M) for 48 h (5 times per 24 h). The mixture was washed with distilled water, centrifuged, and exchanged with MeOH for 24 h (5 times per 24 h). The final



product was collected and dried under dynamic vacuum at 80 °C for 24 h to obtain a pure green powder, termed  $H^+ \subset BUT-8(Cr)$  (80% yield, based on  $Cr^{3+}$ ).  $^1H$ -NMR (digested  $H^+ \subset BUT-8(Cr)$ , DMSO- $d_6$ , 600 MHz):  $\delta$  = 9.57 (s, 2H), and 8.48 (s, 2H), (see ESI† Fig. S1). FT-IR ( $cm^{-1}$ , ATR): 1694 (w), 1614 (s), 1416 (s), 1368 (s), 1216 (w), 1159 (s), 1030 (s), 919 (w), 791 (w), 768 (m), 628 (w).

### Adsorption experiment

All experiments were carried out under a constant stirring rate (300 rpm) and at room temperature. The influences of variables, including the pH, adsorbent dosage, adsorption kinetics, and isotherms, were determined in batch mode. The initial pH was adjusted from 2 to 10 by adding 0.01 M NaOH or HCl solutions using a pH meter. The amount of adsorbent dosage (5–25 mg) was surveyed with the initial concentration of RhB (200 mg  $L^{-1}$ ) to identify the optimal dosage. The adsorption isotherms were determined by observing optimal dosage with different initial concentrations of the RhB dye (25–175 mg  $L^{-1}$ ). The RhB concentrations remaining in the solution after 24 h were analyzed. To investigate the adsorption kinetics, the mixture was continuously stirred with specific intervals from 5 to 150 min. In each experiment, the adsorbent was separated *via* centrifugation to collect the filtrate for determining the remaining RhB concentration using UV-Vis spectrophotometer analysis at a maximum wavelength of 553 nm. The concentration of RhB was confirmed by using a calibration curve made from the standard solutions (Fig. S2, ESI†).

The RhB removal percentage ( $R\%$ ), the equilibrium ( $q_e$ ) and interval adsorption capacity ( $q_t$ ) were determined using the following equations:

$$q_e = \frac{C_o - C_e}{m} \times V \quad (1)$$

$$q_t = \frac{C_o - C_t}{m} \times V \quad (2)$$

$$R\% = \frac{C_o - C_t}{C_o} \times 100 \quad (3)$$

where  $C_o$ ,  $C_e$ , and  $C_t$  are the RhB concentrations at initial, equilibrium time and  $t$ , respectively.  $V$  (mL) is the volume of the dye solution, and  $m$  (mg) is the mass of the used adsorbent.

### Reusability

To evaluate the regeneration of  $H^+ \subset BUT-8(Cr)$ , the adsorption-desorption cycles were performed. In detail, the adsorbed RhB  $\subset BUT-8(Cr)$  material was immersed in ethanol (pH = 7) with constant stirring for 24 h followed by centrifugation to separate the solid from the aqueous medium. The obtained solution was analyzed using a UV-Vis spectrophotometer to inspect if any RhB signal appeared at a wavelength of 553 nm. Then, the separated solid was soaked in ethanol. This process was repeated many times until no signals of RhB were presented. Finally, the desorbed material was collected before vacuum-drying at 80 °C for 24 h and then tested for continuous adsorption studies.

## 3. Results and discussion

### Synthesis and structural characterization of BUT-8(Cr)

In order to confirm the influence of the sulfonic groups within BUT-8(Cr) on the adsorption capacity of RhB, we have fabricated two Cr-based MOF materials, namely MIL-101-NDC and BUT-8(Cr). Accordingly, the structure of MIL-101-NDC crystallizes in the cubic space group of  $Fd-3$ , generated by trimeric  $\{Cr_3(OH)(H_2O)_2(\mu_3-O)\}$  units and unfunctionalized ligand of  $NDC^{2-}$ .<sup>50</sup> MIL-101-NDC contains two kinds of pore windows with diameters of approximately 13.5 and 18.2 Å, respectively. With this feature, MIL-101-NDC is unsuitable for RhB adsorption with ultra-high capacity because of the lack of negatively charged moieties to efficiently uptake the cationic RhB ions. Meanwhile, the structure of BUT-8(Cr) is constructed from the  $Cr_3(\mu_3-O)$  clusters and  $SO_3H$ -functionalized linkers with a cage window of 12.4 Å (Fig. 1). Noteworthy, BUT-8(Cr) adopts densely packed  $SO_3H$  moieties and an appropriate cage window diameter, capable of effectively capturing the positively charged RhB molecules over the framework through robust electrostatic attraction.

The pristine BUT-8(Cr) was fabricated by heating the mixture of  $Cr(NO_3)_3 \cdot 9H_2O$  salt and  $H_4SNDC$  linker in DMF solvent in the presence of hydrofluoric acid as a modulator at 190 °C for 24 h. The phase purity of the as-synthesized BUT-8(Cr) product was demonstrated by powder X-ray diffraction (PXRD) analysis with the typical peaks indexed to (2–10), (2–11), (30–2), and (6–30), which is in good agreement with the simulated BUT-8(Cr) (Fig. 2a). Notably, the dimethylammonium (DMA) ions appeared due to the decomposition of DMF during the reaction process. However, the  $SO_3H$  groups functionalized within BUT-8(Cr) with the anionic forms can effectively balance the positively charged sites of the  $DMA^+$  ions, resulting in the generation of a rigid backbone capable of retaining the structural order.

To recover the sulfonic groups inside BUT-8(Cr) for facilitating the formation of perfect uptake space for RhB adsorption, we performed the exchange of the  $DMA^+$  ions with an excess amount of  $H^+$  ions by immersing the pristine BUT-8(Cr) in 0.3 M  $H_2SO_4$  solution. The material was washed with an abundant amount of distilled water until pH = 5 and then dried under vacuum at 80 °C for 24 h to acquire a new product, denoted as  $H^+ \subset BUT-8(Cr)$ . To demonstrate whether the  $DMA^+$  ions are fully released out of the MOF structure, the activated  $H^+ \subset BUT-8(Cr)$  was digested by the HF medium and dissolved in a  $d_6$ -DMSO solution for  $^1H$ -NMR measurement. As a result, the DMA signals are no longer present in the digested  $H^+ \subset BUT-8(Cr)$  sample (Fig. S1, ESI†). From this, it can be concluded that the exchange process of protons onto BUT-8(Cr) has been successfully conducted. Significantly, the activated  $H^+ \subset BUT-8(Cr)$  has a low crystallinity with broadened diffraction peaks because of the high flexibility of the sulfonic groups (Fig. 2a). This can clearly explain that the guest solvent molecules strongly interact with the sulfonate moieties *via* the hydrogen bonding networks. These solvent molecules will be released from the structure of  $H^+ \subset BUT-8(Cr)$  after activation,



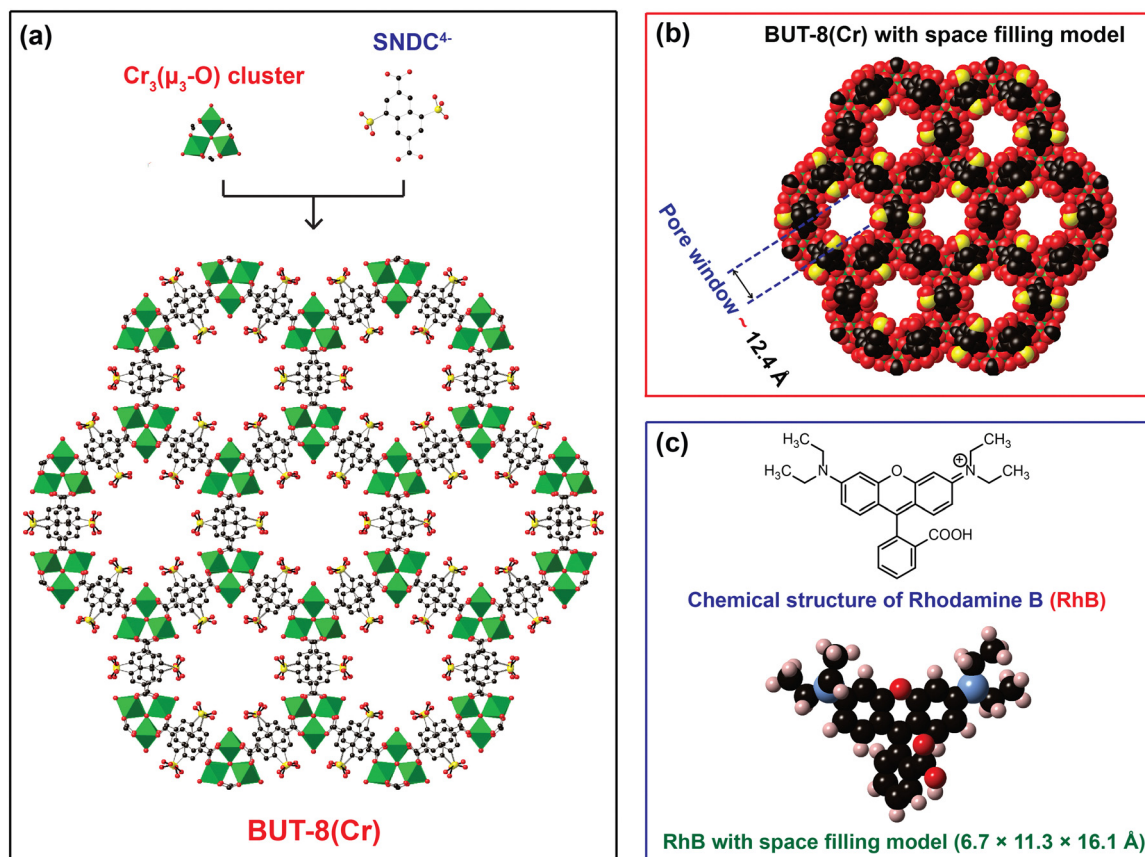


Fig. 1 The structure of  $\text{H}^+ \subset \text{BUT-8(Cr)}$  constructed from the  $\text{Cr}_3(\mu_3\text{-O})$  clusters and  $\text{SNDC}^{4-}$  linker (a); the pore window of BUT-8(Cr) with the space filling model (b); the chemical structure and space filling model of RhB (c). Atom colors: Cr, green polyhedra; C, black; O, red; S, yellow; N, blue. Almost H atoms are omitted for clarity.

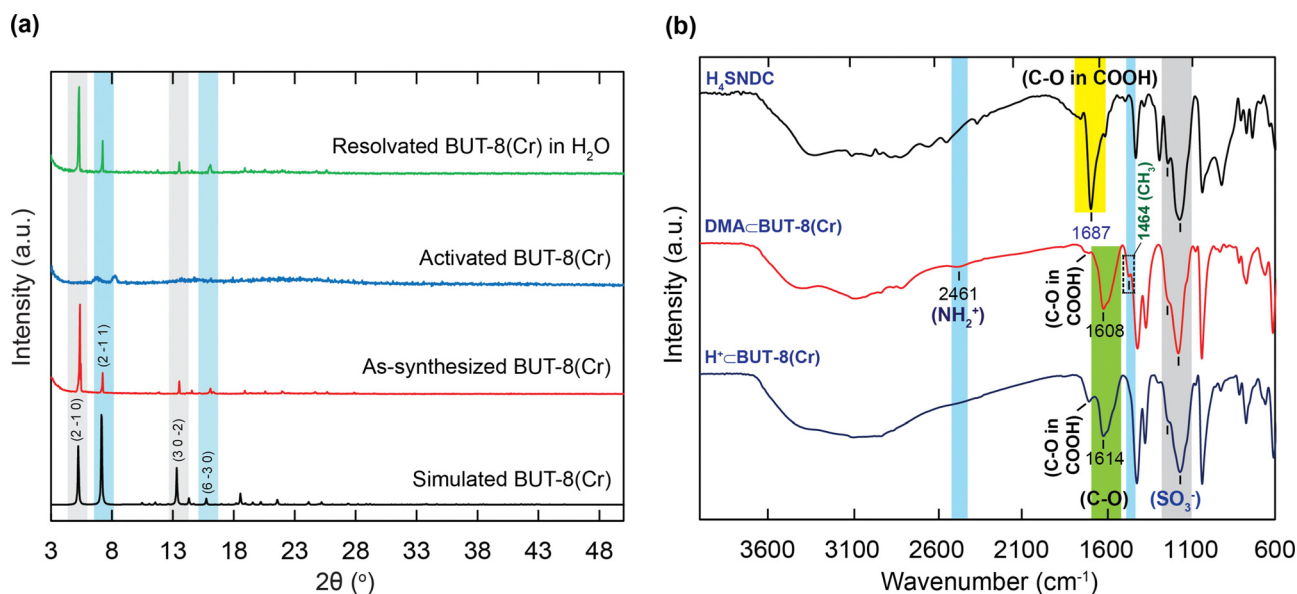


Fig. 2 Powder X-ray diffraction analysis of the as-synthesized DMA- $\subset$ BUT-8(Cr) (red), activated  $\text{H}^+ \subset$ BUT-8(Cr) (blue), and resolved  $\text{H}^+ \subset$ BUT-8(Cr) in water (green) in comparison with simulated BUT-8(Cr) (black) (a); Fourier transform infrared spectra of the  $\text{H}_4\text{SNDC}$  linker (black), DMA- $\subset$ BUT-8(Cr) (red), and  $\text{H}^+ \subset$ BUT-8(Cr) (blue) (b).





leading to a structural order loss. This is also in line with the  $N_2$  adsorption analysis for the  $H^+ \subset BUT-8(Cr)$  (Fig. S8 and S9, ESI<sup>†</sup>); the BET and Langmuir surface areas of the activated  $H^+ \subset BUT-8(Cr)$  (61.41 and 66.77  $m^2 g^{-1}$ , respectively) are much lower than the theoretically predicted value (2751  $m^2 g^{-1}$ , see Fig. S10 and Table S1, ESI<sup>†</sup>).  $H^+ \subset BUT-8(Cr)$  possesses high flexibility upon activation, leading to a significant decrease in the surface area. This situation is also observed with the sulfonic-functionalized MOF materials in the previous reports.<sup>19,40,41,49,51</sup> Interestingly, the PXRD signals appear similar to the simulated structure when the activated  $H^+ \subset BUT-8(Cr)$  is resolvated in water. To demonstrate the promising application under practical conditions, the chemical stability of  $H^+ \subset BUT-8(Cr)$  was tested by immersing it in an aqueous medium. Accordingly, the structural order of the material is retained after being soaked in water for 30 days, as evidenced from the PXRD analysis results (Fig. S11, ESI<sup>†</sup>).

Next, the FT-IR spectra of  $DMA \subset BUT-8(Cr)$  and  $H^+ \subset BUT-8(Cr)$  (Fig. 2b) show the signals at 1178  $cm^{-1}$  and 1190  $cm^{-1}$ , which can be assigned to the presence of the  $SO_3^-$  functional group in the  $H_4SNDC$  linker and both types of  $BUT-8(Cr)$ . This result indicates the  $SO_3^-$  functionalization into the  $BUT-8(Cr)$  materials. Furthermore, the bands of C–O in the carboxylate group of  $DMA \subset BUT-8(Cr)$  and  $H^+ \subset BUT-8(Cr)$  are at 1614  $cm^{-1}$  and 1608  $cm^{-1}$ , respectively, reflecting the lower vibrational frequency of this band in the carboxylate group of  $H_4SNDC$  (1687  $cm^{-1}$ ). It is realized that the resonance in the carboxylate group causes the bond multiplicity to decrease. Thus the wavenumber tends to be lower than the initial signals. The peaks at 2461  $cm^{-1}$  and 1464  $cm^{-1}$  recorded for the  $DMA \subset BUT-8(Cr)$  sample are attributed to the presence of  $-NH_2^+$  and  $-CH_3$  groups in  $(CH_3)_2NH_2^+$ , which are absent in the sample of  $H^+ \subset BUT-8(Cr)$ .

Additionally, the EDX-mapping data of  $H^+ \subset BUT-8(Cr)$  have also revealed the absence of nitrogen element, showing that all

of the  $DMA^+$  ions are completely removed. In fact, both the  $H^+$  and  $DMA^+$  ions can freely diffuse inside and outside the pores of the material (Fig. S3, ESI<sup>†</sup>). The surface morphology of  $H^+ \subset BUT-8(Cr)$  is characterized by SEM and TEM images (Fig. S4 and S5, ESI<sup>†</sup>), which show that  $H^+ \subset BUT-8(Cr)$  crystallizes as globular particles with a size of approximately 2  $\mu m$  and possess a high agglomeration of the particles. This leads to the difficult observation of the porous texture of the MOF particles from the TEM data.

For further studies on the thermal stability of the material, thermal gravimetric analysis (TGA) was also conducted on the activated samples, including the  $DMA \subset BUT-8(Cr)$ ,  $H^+ \subset BUT-8(Cr)$ , and  $RhB \subset BUT-8(Cr)$  samples. The TGA curves are measured under dry air and are illustrated in Fig. 3a. In detail, two weight losses can be observed from these three samples, before 300 °C and between 300 and 700 °C, respectively. The first step, with approximately 5 wt% weight loss, can be assigned to the evaporation of the coordinated and absorbed water molecules. The second step with significant weight loss (*ca.* 57–60 wt%) can be attributed to the release of the  $RhB$  molecules and the decomposition of the framework of all samples. As a result,  $BUT-8(Cr)$  has high thermal stability up to 300 °C, which opens promising adsorption applications under practical conditions.

In order to gain deeper insight into the influence of the number of sulfonic moieties within the MOF backbone on the  $RhB$  uptake capacity, a series of experiments were performed. Consequently, 10 mg of each, MIL-101-NDC,  $DMA \subset BUT-8(Cr)$ , and  $H^+ \subset BUT-8(Cr)$ , is introduced into 100 mL of various  $RhB$  solutions with an initial concentration range of 20 to 160  $mg L^{-1}$  at a pH value of 3. As a consequence, the  $RhB$  adsorption capacities at 160  $mg L^{-1}$  concentration on MIL-101-NDC,  $DMA \subset BUT-8(Cr)$ , and  $H^+ \subset BUT-8(Cr)$  are 98.3, 318.6, and 756.9  $mg g^{-1}$ , respectively (Fig. 3b).

It is realized that the increase in the  $RhB$  uptake in the presence of a large amount of  $SO_3H$  groups within the structure

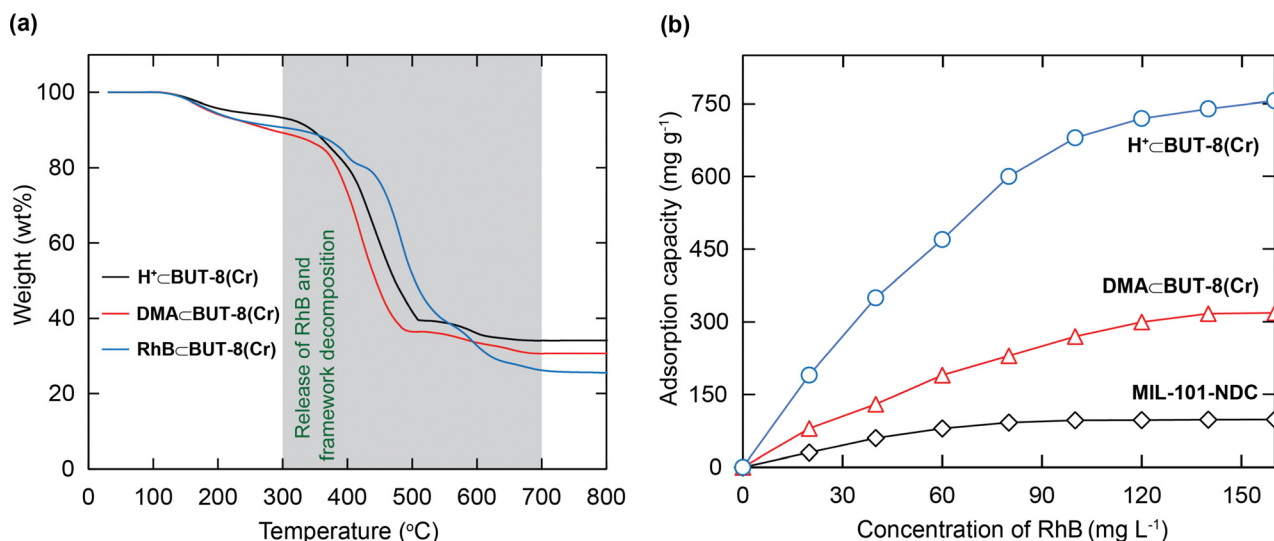


Fig. 3 (a) TGA curves of activated  $H^+ \subset BUT-8(Cr)$  (black), activated  $DMA \subset BUT-8(Cr)$  (red), and activated  $RhB \subset BUT-8(Cr)$  (blue); (b) dependence of the sulfonic groups within the structures of MIL-101-NDC,  $DMA \subset BUT-8(Cr)$  and  $H^+ \subset BUT-8(Cr)$  on the  $RhB$  adsorption capacity.



of  $\text{H}^+ \subset \text{BUT-8(Cr)}$  can be ascribed to the increased electrostatic interaction between the cationic RhB ions and the formation of  $\text{SO}_3^-$  in the pores of the material.  $\text{DMA} \subset \text{BUT-8(Cr)}$  displays a lower adsorption capacity of RhB than  $\text{H}^+ \subset \text{BUT-8(Cr)}$  due to the presence of  $\text{DMA}^+$  ions preventing the entry of the RhB molecules into the pores. Meanwhile, MIL-101-NDC exhibits the lowest adsorption capacity for RhB because of the lack of sulfonic moieties within its framework. Following the gained data, we choose the  $\text{H}^+ \subset \text{BUT-8(Cr)}$  material to study the further adsorption experiments of RhB in this work.

### Influence of pH and ionic strength

To explore the effect of pH on the RhB capture from the solution, initial pH values ranging from 2 to 10 affecting the uptake performance of RhB were surveyed. It can be understood from Fig. 4a that the highest RhB adsorption capacity was recorded at  $\text{pH} = 3$  and it decreased when the pH values increased. This tendency can be explained through efficient electrostatic interaction between the  $\text{SO}_3^-$  groups and the positively charged  $\text{RhB}^+$  ions. At low pH values, two main processes occur in the solution such as the ionization of RhB to form the cationic RhB ions and the protonation process of  $\text{SO}_3^-$  moieties to generate the  $\text{SO}_3\text{H}$  or  $\text{SO}_3\text{H}_2^+$  species.<sup>52</sup> These transformation processes lead to the repulsion force or weak interaction between the cationic RhB dye and the protonated forms. However, at higher pH values, the neutral form of RhB is formed through the zwitter ion equilibrium;<sup>52</sup> meanwhile  $\text{SO}_3^-$  components still existed in this form, which leads to less occupation between the active sites and the adsorbent, resulting in the low uptake of the RhB dye. At  $\text{pH} = 3$ , a balanced point between these contradictory circumstances is achieved. With all of this considered, the pH value of 3 is selected as an optimal pH value for the subsequent studies. Also, the RhB adsorption onto  $\text{H}^+ \subset \text{BUT-8(Cr)}$  is weakly dependent on the ionic strength with different solutions of 0.1 M and 0.01 M

NaCl. Thus it can be concluded that the adsorption of RhB over the material depends on the inner-sphere complexation *via* the electrostatic attraction between the sulfonate groups and  $\text{RhB}^+$  ions rather than the outer-sphere surface complexation.<sup>53</sup>

### Effect of adsorbent dose

To determine the optimal dosage of the adsorbent for enhancing the interaction between the adsorption regions within  $\text{H}^+ \subset \text{BUT-8(Cr)}$  and the RhB molecules, different amounts of activated  $\text{H}^+ \subset \text{BUT-8(Cr)}$  (5–25 mg) were added to 100 mL of  $\text{Pb}^{2+}$  solution ( $100 \text{ mg L}^{-1}$ ) at  $\text{pH} = 3$  and stirred for 24 h. As shown in Fig. 4b, the adsorption capacity strongly increased from  $530 \text{ mg g}^{-1}$  to  $630 \text{ mg g}^{-1}$ , approximately, as the  $\text{H}^+ \subset \text{BUT-8(Cr)}$  content increased from 5 to 10 mg, respectively. It is clear to note that the larger mass of the material has opened up more available adsorption space with more effective interaction through adsorption sites. However, the data on adsorption capacity do not show any significant increase when the  $\text{H}^+ \subset \text{BUT-8(Cr)}$  mass varies from 15 to 25 mg. This circumstance reveals that the adsorption process has reached the equilibrium point. Hence, the adsorption content of 10 mg is selected as the optimum condition of the material content.

### Adsorption isotherms

To elucidate the RhB adsorption properties of  $\text{H}^+ \subset \text{BUT-8(Cr)}$ , the adsorption isotherm models were used to illustrate the attraction between the  $\text{RhB}^+$  ions and the adsorbent specifically. On varying the RhB concentration in the range of 25 to  $175 \text{ mg L}^{-1}$ , the adsorption uptake of RhB promptly increases with an increase in the initial concentration of RhB. It approaches a maximum adsorption capacity ( $q_m$ ) of  $811.7 \text{ mg g}^{-1}$ , as shown in Fig. 5a. This is attributed to the appearance of more dense adsorption sites available on  $\text{H}^+ \subset \text{BUT-8(Cr)}$ . The obtained results reveal that the active ranges of  $\text{H}^+ \subset \text{BUT-8(Cr)}$  are the limiting components for the uptake process of RhB.

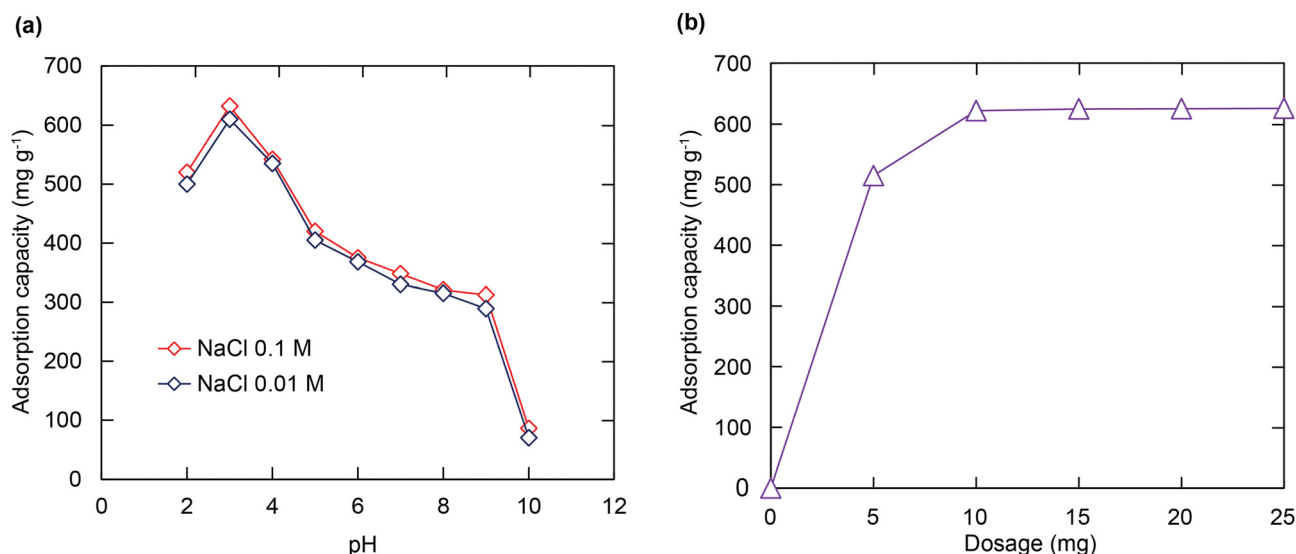


Fig. 4 Influence of solution pH value and ionic strength on the adsorption capacity of RhB over  $\text{H}^+ \subset \text{BUT-8(Cr)}$  [ $m = 10 \text{ mg}$ ,  $C_0 = 200 \text{ mg L}^{-1}$ ,  $V_{\text{RhB}} = 50 \text{ mL}$ ,  $t = 24 \text{ h}$ ] (a); Effect of  $\text{H}^+ \subset \text{BUT-8(Cr)}$  content on the RhB adsorption uptake [ $m$ : 5–25 mg,  $C_0 = 200 \text{ mg L}^{-1}$ ,  $V_{\text{RhB}} = 100 \text{ mL}$ ,  $\text{pH} = 3$ ,  $t = 24 \text{ h}$ ] (b).

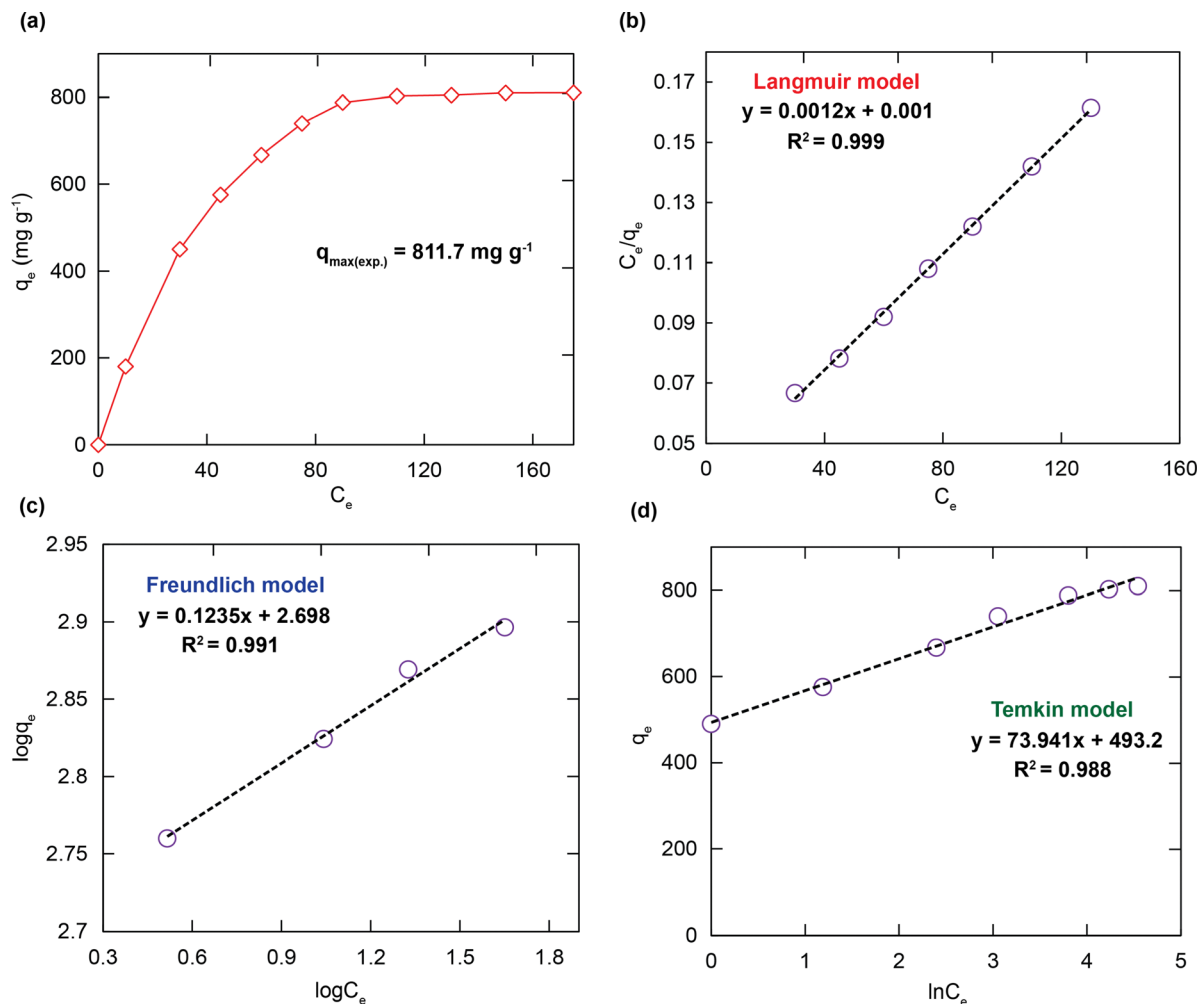


Fig. 5 Effect of the concentration of RhB on the adsorption capacity of  $H^+$  c-BUT-8(Cr) [ $m = 10$  mg,  $V_{\text{RhB}} = 100$  mL,  $C_o$ : 25–175  $\text{mg L}^{-1}$ , pH = 3,  $t = 24$  h] (a); fitting results with the adsorption isotherm models: Langmuir (b), Freundlich (c), and Temkin (d).

To interpret the adsorption mechanism of RhB over the material, the adsorption isotherm models such as Langmuir, Freundlich, and Temkin were employed. The linear forms of these models are displayed in the eqn (S1)–(S3) (ESI†). For further application of Langmuir adsorption isotherm models, uniform surface area and monolayer adsorption with limited active sites are assumed. The Freundlich model is applied with the assumption that adsorption processes happen on heterogeneous surfaces generated from the existence of functional groups and interactions between the adsorbent and adsorbate. The Temkin model is applied with the assumption that adsorption heat of all molecules is not involved in a straight line.<sup>54</sup>

As shown in Fig. 5b–d and Table 1, the calculated  $R^2$  value for fitting in the Langmuir model (0.999) is higher than those in the Freundlich model (0.991) and Temkin model (0.988). The theoretical adsorption capacity of RhB estimated from the compatible model is  $833.3 \text{ mg g}^{-1}$ , which is much more appropriate than the experimental value of  $811.7 \text{ mg g}^{-1}$  previously. It can be extrapolated that the material  $H^+$  c-BUT-8(Cr) has a uniform distribution of various active sites and

Table 1 The parameters calculated from isotherm models for the adsorption of RhB onto  $H^+$  c-BUT-8(Cr)

Isotherm models	Parameters	Value
Langmuir	$q_m (\text{mg g}^{-1})$	833.3
	$K_L (\text{L mg}^{-1})$	1.201
	$R^2$	0.999
Freundlich	$1/n$	0.114
	$K_F (\text{mg g}^{-1} (\text{L g}^{-1})^{1/n})$	501.2
	$R^2$	0.991
Temkin	$K_T (\text{L mg}^{-1})$	788.5
	$\beta$	33.51
	$R^2$	0.988

monolayer adsorption proves to be more powerful. Besides, the separation factor of  $R_L$  value (determined using the eqn (S4), ESI†), is obtained to be greater than zero and smaller than 1. These results are appropriate with the chemical adsorption, which is caused by the electrostatic interaction between negatively charged  $\text{SO}_3^-$  moieties and the cationic RhB dye and  $\pi$ – $\pi$  interaction between the aromatic rings of the structure of the organic ligand and the RhB molecules.<sup>40,41,51,55</sup>



### Adsorption kinetics

As illustrated in Fig. 6a, the ultra-fast RhB capacity is confirmed through a contact time of 15 minutes to be approximately  $620 \text{ mg g}^{-1}$ . It is noted that fast removal is promising for overcoming the limitations of traditional adsorbents, leading to a possibility of effectively working in a real aqueous medium. The chemical interaction and diffusion rate are two main elements responsible for the adsorption properties of  $\text{H}^+ \text{C-BUT-8(Cr)}$ . Consequently, the adsorption capability of this material was surveyed at specific times, with optimum conditions chosen from the previous examination. The gained data were analyzed through pseudo first order, pseudo second order, and intra-particle diffusion models.

In general, the pseudo first order model assumes that the adsorption rate is decided by the surface, which can be illustrated in a linear form as follows:

$$\ln(q_e - q_t) = \ln q_e - k_1 t \quad (4)$$

where  $q_t$  and  $q_e$  are the RhB adsorption capacity at  $t$  and equilibrium of  $\text{H}^+ \text{C-BUT-8(Cr)}$  and  $k_1$  ( $\text{g mg}^{-1} \text{ min}^{-1}$ ) is the

rate constant of pseudo first order. If  $\ln(q_e - q_t)$  and  $t$  are relevant in a linear form with the  $R^2$  value being approximately 1, the adsorption process can be considered to fit this model.<sup>51,54</sup> The pseudo second order model is supposed to show that the adsorption is caused by the interactions between the functional groups of the material and the adsorbates. The rearrangement shows the original relationship of the rate law to obtain a linear form as follows:

$$\frac{t}{q_t} = \frac{1}{k_2 q_e^2} + \frac{t}{q_e} \quad (5)$$

The linear equation of the intra-particle diffusion model can be written as follows:

$$q = k_3 t^{1/2} + c \quad (6)$$

Where  $k_3$  ( $\text{g mg}^{-1} \text{ min}^{-1}$ ) and  $c$  ( $\text{mol L}^{-1}$ ) are the rate constant of intraparticle diffusion and the initial RhB concentration, respectively.<sup>34,47</sup>

As shown in Fig. 6b, c and Table 2, it is clear to note that the pseudo first order model is not acceptable for studying the RhB

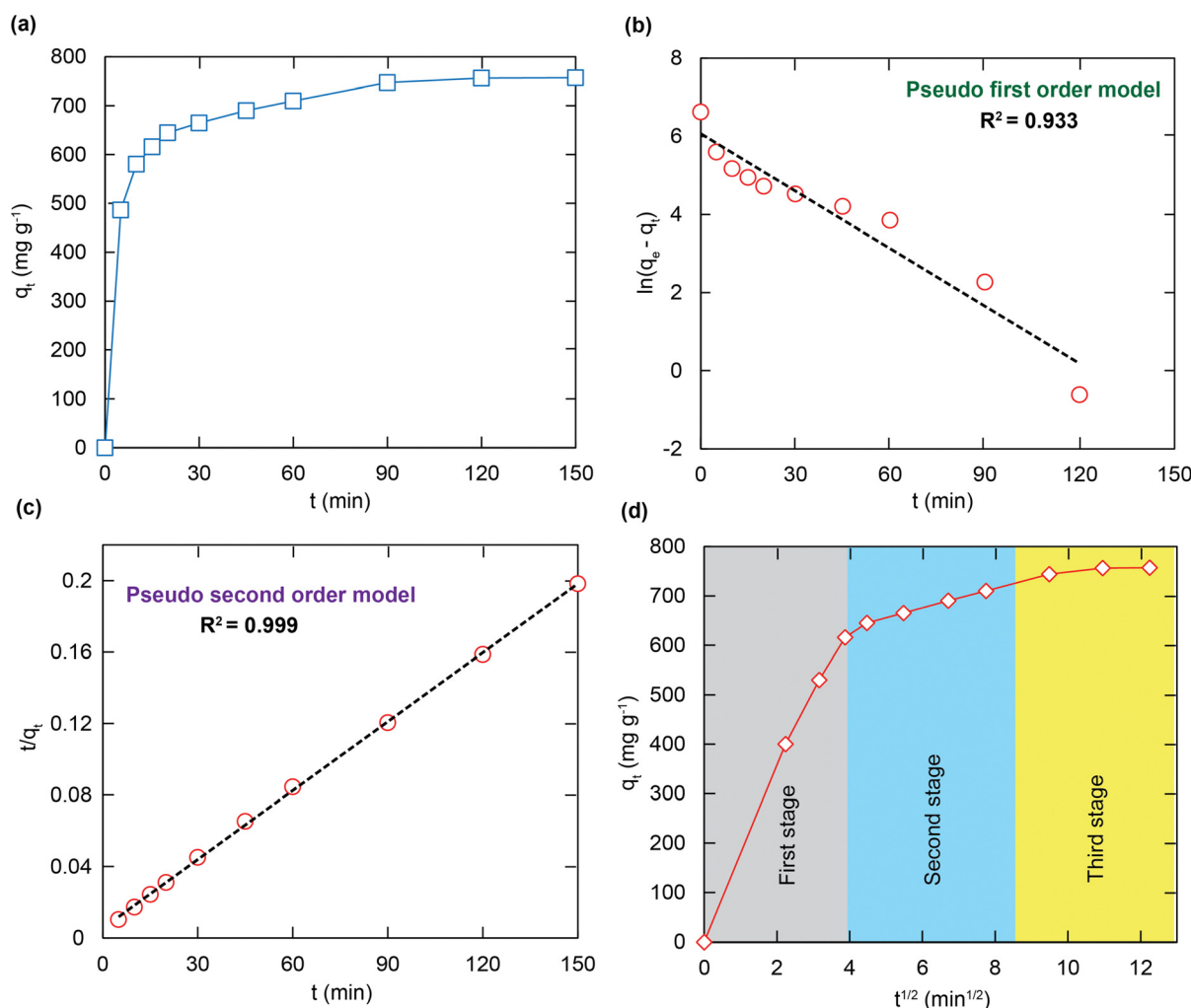


Fig. 6 The kinetic curve for the adsorption of RhB onto  $\text{H}^+ \text{C-BUT-8(Cr)}$  [ $m = 10 \text{ mg}$ ,  $V_{\text{RhB}} = 100 \text{ mL}$ ,  $C_0 = 100 \text{ mg L}^{-1}$ ,  $\text{pH} = 3$ ] (a); data fitting with the adsorption kinetic models: pseudo first order (b), pseudo second order (c) and intra-particle diffusion model (d).



**Table 2** The parameters of the removal kinetics and adsorption capacities of  $\text{H}^+ \subset \text{BUT-8}(\text{Cr})$  for the RhB adsorption

Kinetic models	Parameters	Value
Pseudo first order	$q_{\text{e,exp}} (\text{mg g}^{-1})$	811.7
	$q_{\text{e,cal}} (\text{mg g}^{-1})$	266.1
	$k_1 (\text{min}^{-1})$	0.014
	$R^2$	<b>0.933</b>
Pseudo second order	$q_{\text{e,cal}} (\text{mg g}^{-1})$	769.2
	$k_2 (\text{g mg}^{-1} \text{min}^{-1}) \times 10^{-4}$	3.131
	$R^2$	<b>0.999</b>

adsorption kinetics onto  $\text{H}^+ \subset \text{BUT-8}(\text{Cr})$  ( $R^2 = 0.933$ ). Meanwhile, the correlation coefficient of  $R^2$  is calculated as 0.999 while fitting to the pseudo second order model, obviously suitable for this adsorption process. Also, the calculated RhB adsorption capacity at equilibrium is  $769.2 \text{ mg g}^{-1}$ , approximately, which is closely correlated with the experimental value of  $811.7 \text{ mg g}^{-1}$ . Therefore, the RhB adsorption onto  $\text{H}^+ \subset \text{BUT-8}(\text{Cr})$  is a chemisorption process through two main interactions: the electrostatic attraction between the RhB<sup>+</sup> ions and  $\text{SO}_3^-$  components within the framework and the  $\pi$ - $\pi$  stacking.<sup>55–57</sup>

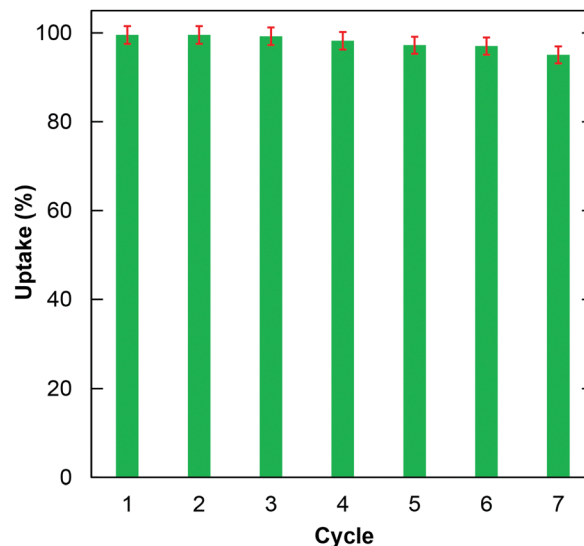
According to Fig. 6d, the adsorption process can be divided into three stages, with the rate constant values growing from  $k_{i1}$  to  $k_{i3}$ . It should be noted that the difference in the RhB diffusion rate was the cause of this decreasing trend. In detail, at the first stage, the RhB molecules diffuse very fast from the solution to the outer surface until becoming fully soaked. Next, the adsorbate molecules turn to move to the inner space surface with an increase in the diffusion resistance. Then, the RhB molecules move inside the pores of  $\text{H}^+ \subset \text{BUT-8}(\text{Cr})$  at a lower speed, and simultaneously have electrostatic and  $\pi$ - $\pi$  interaction with the functional groups of the framework until the equilibrium point is reached.<sup>40</sup>

### Regeneration study

The reusability of the material is considered one of the determining factors for better performance. Herein, the reusability of  $\text{H}^+ \subset \text{BUT-8}(\text{Cr})$  in the RhB adsorption was investigated for seven cycles. The result in Fig. 7 indicates that the RhB uptake only decreases to 94.5% after seven cycles.

In particular, the successful regeneration of  $\text{H}^+ \subset \text{BUT-8}$  was proved using the FTIR spectra and PXRD analysis. Accordingly, there is good agreement in the PXRD patterns of  $\text{H}^+ \subset \text{BUT-8}(\text{Cr})$  products before and after the desorption of RhB (Fig. S6, ESI†). The characteristic bands of  $\text{H}^+ \subset \text{BUT-8}(\text{Cr})$  after desorption are almost unchanged in comparison with the activated  $\text{H}^+ \subset \text{BUT-8}(\text{Cr})$  (Fig. S7, ESI†). These findings illustrated that the  $\text{H}^+ \subset \text{BUT-8}(\text{Cr})$  material could be utilized as a reusable material to eliminate toxic organic dyes from wastewater.

To verify the feasibility of the material, the maximum RhB adsorption capacity of  $\text{H}^+ \subset \text{BUT-8}(\text{Cr})$  was compared with those of other MOF materials (Table 3). The data reveal that  $\text{H}^+ \subset \text{BUT-8}(\text{Cr})$  has a larger adsorption capacity than the other materials despite not having a rigid structure *via* the effective

**Fig. 7** The reusability of  $\text{H}^+ \subset \text{BUT-8}(\text{Cr})$  in the RhB uptake process.**Table 3** Summary of the maximum RhB adsorption capacity of  $\text{H}^+ \subset \text{BUT-8}(\text{Cr})$  and other related MOF materials

Material	$q_{\text{max}} (\text{mg g}^{-1})$	Ref.
Zn-MOF	3.8	58
$\text{Fe}_3\text{O}_4/\text{MIL-100}(\text{Fe})$	28.4	59
$\text{MgFe}_2\text{O}_4/\text{MOF}$	219.8	60
USTC-1	13.4	61
POM@UiO-66	28.4	62
MIL-125(Ti)	59.9	63
In-MOF@GO	267.0	64
MIL-101-NDC	98.3	This work
DMA $\subset$ BUT-8(Cr)	318.6	
$\text{H}^+ \subset \text{BUT-8}(\text{Cr})$	811.7	

interaction of the cationic RhB ion with the  $\text{SO}_3^-$  moieties inside  $\text{H}^+ \subset \text{BUT-8}(\text{Cr})$ . This indicates that the  $\text{SO}_3^-$  groups at the internal surface and channel wall of the  $\text{H}^+ \subset \text{BUT-8}(\text{Cr})$  play a vital role in the RhB capture.

### Possible adsorption mechanism

The excellent adsorption performance inspired us to gain a further understanding of the interaction between the active sites within the MOF and the RhB molecules *via* the analyses of the FT-IR spectra, Raman spectra, PXRD patterns, and TGA-DSC curves.

The FT-IR spectrum of RhB  $\subset$  BUT-8(Cr) indicates that the characteristic bands of the C–O and S–O shifted to the lower wavenumber ranges at  $1604$  and  $1153 \text{ cm}^{-1}$ , respectively (Fig. 8a). These data show efficient attraction between the  $\text{SO}_3^-$  groups and the RhB<sup>+</sup> ions, driving the generation of the strong ionic bonds of the RhB with sulfonic groups. This situation is in good accordance with the previous studies.<sup>19,40,41</sup>

Moreover, Raman spectra of RhB  $\subset$  BUT-8(Cr) are analyzed and are shown in Fig. 8b. The new vibrational modes are also



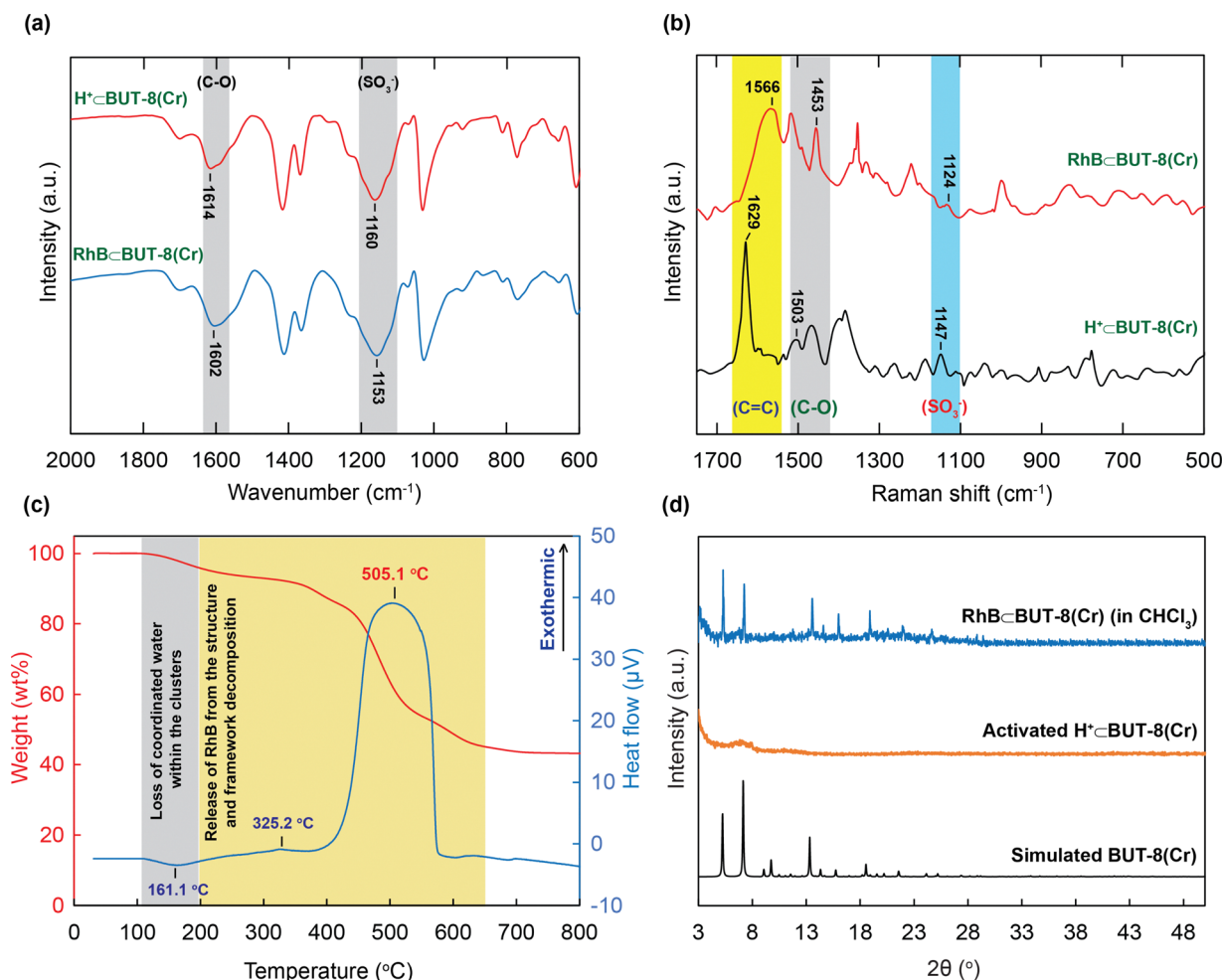


**Fig. 8** Fourier transform infrared spectra of RhB-BUT-8(Cr) (blue) as compared to those of H<sup>+</sup>-BUT-8(Cr) (red) (a); Raman spectra of RhB-BUT-8(Cr) (red) in comparison with those of H<sup>+</sup>-BUT-8(Cr) (black) (b); TGA diagram (red) and DSC curve (blue) of activated RhB-BUT-8(Cr) (c); powder X-ray diffraction analysis of RhB-BUT-8(Cr) (RhB solution with CHCl<sub>3</sub>) (blue), activated H<sup>+</sup>-BUT-8(Cr) (orange) in comparison with simulated BUT-8(Cr) (black) (d).

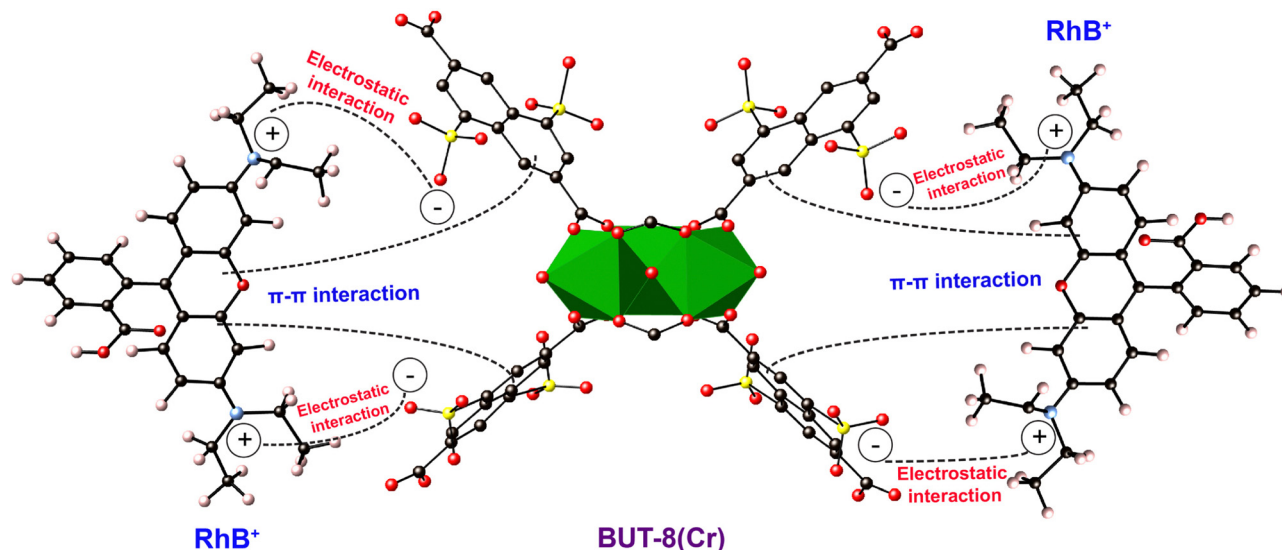
observed at 1453 and 1124 cm<sup>-1</sup>, relating to the characteristic frequencies of C-O and S-O, which appear in the RhB-BUT-8(Cr) spectrum, but are found at other positions in the H<sup>+</sup>-BUT-8(Cr) sample. This result again demonstrates the effective electrostatic interaction of the positively charged RhB ions and anionic SO<sub>3</sub><sup>-</sup> sites (Scheme 1). In addition, the band derived from the vibration of C=C in the benzene ring of RhB-BUT-8(Cr) appears at 1566 cm<sup>-1</sup> in comparison with that of H<sup>+</sup>-BUT-8(Cr). This can be accounted for the formation of the  $\pi$ - $\pi$  stacking attraction *via* the interaction between the conjugated planar of the benzene rings of the ligands within MOFs and the RhB molecules (Scheme 1).<sup>41,65</sup>

Besides, the appearance of the RhB dyes inside H<sup>+</sup>-BUT-8(Cr) was verified using the TGA-DSC curve recorded under dry air. As illustrated in Fig. 8c, the TGA-DSC diagram indicates a weight loss of 6.5 wt% from 25 to 250 °C with a specific endothermic peak at 161.1 °C. This is assigned to the loss of coordinated water inside the MOF clusters. From 250 to 700 °C, a huge weight loss is observed and identified for the release of

the RhB dyes from the material and the structural decomposition, which are verified using the exothermic peaks appearing at 325.2 and 505.1 °C.

To further prove the mentioned  $\pi$ - $\pi$  interactions, H<sup>+</sup>-BUT-8(Cr) is soaked in the RhB solution containing a non-polar solvent such as chloroform (CHCl<sub>3</sub>). Here, using the CHCl<sub>3</sub> solvent can support the formation process of the neutral states within BUT-8(Cr) and the RhB molecules. In general, the crystallinity of the activated H<sup>+</sup>-BUT-8(Cr) material disappears after activation. Therefore, we expect that if the RhB dyes are loaded into the structure of BUT-8(Cr), the structural order of the material will retain upon activation. Consequently, the PXRD patterns are collected to inspect whether the RhB molecules have entered into the architecture of BUT-8-Cr. As expected, the PXRD analysis of activated RhB-BUT-8(Cr) (immersed in CHCl<sub>3</sub>) is in good accordance with the simulated BUT-8(Cr). This can demonstrate that the neutral RhB dyes are anchored over the structure of H<sup>+</sup>-BUT-8(Cr) through  $\pi$ - $\pi$  stacking interactions (Fig. 8d).





**Scheme 1** The plausible adsorption mechanism of  $\text{RhB}^+$  onto BUT-8(Cr). Atom colors: Cr, green polyhedra; C, black; O, red; S, yellow; N, blue.

## 4. Conclusion

In summary, a sulfonic-functionalized Cr-based metal–organic framework was successfully synthesized and studied for its adsorption performance in the RhB capture process. It is clear to note that the maximum adsorption capacity for the RhB dye over  $\text{H}^+$  BUT-8(Cr) is gained to be  $811.7 \text{ mg g}^{-1}$ . This obtained result is much higher than those of the previously reported MOF materials. The data from the adsorption isotherm and kinetic investigations indicate that the RhB adsorption is a chemical process and can be described using the Langmuir isotherm and the pseudo second order models. Moreover, the regeneration experiments show a high removal rate in recycling the material for at least seven cycles. Notably, the adsorption mechanism is elucidated by the experimental analyses. The result reveals that the adsorption mechanism can be depicted in the formation of the chemical bonds *via* electrostatic attraction between the negatively charged sulfonate moieties and the cationic RhB ions and  $\pi$ – $\pi$  stacking interaction of the conjugated  $\pi$  planar in the system of benzene rings. This exploration demonstrates that the Cr-sulfonic-based MOF exhibits remarkable potential for employment in the removal of the RhB dye from wastewater.

## Author contributions

M. V. N. formulated this project. M. V. N., K. M. V. N., A. V. N. P., N. T. D., T. Q. T., H. K. D., and H. N. N. synthesized the compounds and collected isotherms, powder X-ray diffraction patterns, FT-IR spectra, and TGA-DSC curves. M. V. N. wrote the paper and all authors contributed to revising it. All authors have given approval to the final version of the manuscript.

## Conflicts of interest

The authors maintain that they have no conflict of interest for this communication.

## Acknowledgements

My V. Nguyen gratefully acknowledges the support of this work under the funding of the Ministry of Education and Training, Vietnam, through Grant No. B2023-SPS-07. The project entitled: “Synthesis and evaluation of the adsorption and photocatalytic ability of water-stable MOFs material” (Tong hop va danh gia kha nang hap phu, quang xuc tac cua vat lieu MOFs ben nuoc).

## References

- 1 A. K. Al-Buriahi, A. A. Al-Gheethi, P. S. Kumar, R. M. S. R. Mohamed, H. Yusof, A. F. Alshalif and N. A. Khalifa, *Chemosphere*, 2022, **287**, 132162.
- 2 M. Soylak, Y. Unsal, E. Yilmaz and M. Tuzen, *Food Chem. Toxicol.*, 2011, **49**, 1796–1799.
- 3 H. Tong, Q. Jiang, X. Zhong and X. Hu, *Environ. Sci. Pollut. Res.*, 2021, **28**, 4209–4215.
- 4 M. T. Yagub, T. K. Sen, S. Afroze and H. M. Ang, *Adv. Colloid Interface Sci.*, 2014, **209**, 172–184.
- 5 H. Xue, Q. Chen, F. Jiang, D. Yuan, G. Lv, L. Liang, L. Liu and M. Hong, *Chem. Sci.*, 2016, **7**, 5983–5988.
- 6 Y. C. Wong, Y. S. Szeto, W. H. Cheung and G. McKay, *Process Biochem.*, 2004, **39**, 693–702.
- 7 D. R. Sulistina and S. Martini, *Am. J. Public Health Res.*, 2020, **9**, 101–104.
- 8 R. Jain, M. Mathur, S. Sikarwar and A. Mittal, *J. Environ. Manage.*, 2007, **85**, 956–964.
- 9 E. Baldev, D. MubarakAli, A. Ilavarasi, D. Pandiaraj, K. A. S. S. Ishack and N. Thajuddin, *Colloids Surf., B*, 2013, **105**, 207–214.
- 10 S. Jonjana, A. Phuruangrat, N. Ekthammathat, S. Thongtem and T. Thongtem, *J. Electron. Mater.*, 2019, **48**, 4789–4796.
- 11 A. I. Adeogun and R. B. Balakrishnan, *Appl. Water Sci.*, 2017, **7**, 1711–1723.



- 12 G. Yang, D. Zhang, G. Zhu, T. Zhou, M. Song, L. Qu, K. Xiong and H. A. Li, *RSC Adv.*, 2020, **10**, 8540–8547.
- 13 B. Cuiping, X. Xianfeng, G. Wenqi, F. Dexin, X. Mo, G. Zhongxue and X. Nian, *Desalination*, 2011, **278**, 84–90.
- 14 R. Rathinam and S. Pattabhi, *Indian J. Ecol.*, 2019, **46**, 167–174.
- 15 K. Rakesh, S. C. Mohan, S. Karuppuchamy and K. Jothivenkatachalam, *J. Environ. Chem. Eng.*, 2018, **6**, 3610–3620.
- 16 J. Ji, Y. Liu, X. Yang, J. Xu and X. Li, *J. Environ. Manage.*, 2018, **218**, 300–308.
- 17 A. Baddouh, G. G. Bessegato, M. M. Rguiti, B. E. Ibrahimi, L. Bazzi, M. Hilali and M. V. B. Zanon, *J. Environ. Chem. Eng.*, 2018, **6**, 2041–2047.
- 18 Y. Miyah, A. Lahrichi, M. Idrissi, A. Khalil and F. Zerrouq, *Surf. Interfaces*, 2018, **11**, 74–81.
- 19 M. V. Nguyen, H. N. Nguyen, T. A. T. Nguyen and K. M. V. Nguyen, *RSC Adv.*, 2022, **12**, 30201–30212.
- 20 N. Wang, Y. F. Wang, A. M. Omer and X. K. Ouyang, *Anal. Bioanal. Chem.*, 2017, **409**, 6643–6653.
- 21 T. Wu, X. Cai, S. Tan, H. Li, J. Liu and W. Yang, *Chem. Eng. J.*, 2011, **173**, 144–149.
- 22 L. Huang, X. Weng, Z. Chen, M. Megharaj and R. Naidu, *Spectrochim. Acta, Part A*, 2014, **130**, 295–301.
- 23 T. M. Alslaiibi, I. Abustan, M. A. Ahmad and A. A. Foul, *J. Chem. Technol. Biotechnol.*, 2013, **88**, 1183–1190.
- 24 P. K. Malik, *J. Hazard. Mater.*, 2004, **113**, 81–88.
- 25 K. Porkodi and K. V. Kumar, *J. Hazard. Mater.*, 2007, **143**, 311–327.
- 26 K. Y. Kumar, H. B. Muralidhara, Y. A. Nayaka, J. Balasubramanyam and H. Hanumanthappa, *Powder Technol.*, 2013, **246**, 125–136.
- 27 S. K. Das, J. Bhowal, A. R. Das and A. K. Guha, *Langmuir*, 2006, **22**, 7265–7272.
- 28 S. Ranjbari, A. Ayati, B. Tanhaei, A. Al-Othman and F. Karimi, *Environ. Res.*, 2022, **204**, 111961.
- 29 S. M. Khoshkho, B. Tanhaei, A. Ayati and M. Kazemi, *J. Mol. Liq.*, 2021, **324**, 115118.
- 30 S. H. Tabrizi, B. Tanhaei, A. Ayati and S. Ranjbari, *Environ. Res.*, 2022, **204**, 111965.
- 31 X. Wang, Y. Guo, Z. Jia, H. Ma, C. Liu, Z. Liu, Q. Shi, B. Ren, L. Li, X. Zhang and Y. Hu, *Desalination*, 2021, **516**, 115220.
- 32 E. Alver and A. Ü. Metin, *Chem. Eng. J.*, 2012, **200**, 59–67.
- 33 Q. L. Zhu and Q. Xu, *Chem. Soc. Rev.*, 2014, **43**, 5468–5512.
- 34 H. C. Zhou, J. R. Long and O. M. Yaghi, *Chem. Rev.*, 2012, **112**, 673–674.
- 35 L. M. Wang, W. Y. Liu, M. L. Hu, J. S. Yao, P. Wang, J. H. Liu, M. He, Y. Gao and Z. X. Li, *Rare Met.*, 2022, **41**, 2701–2710.
- 36 Y. M. Lin, H. S. Fan, C. Z. Zhu and J. Xu, *Rare Met.*, 2022, **41**, 4104–4115.
- 37 Y. F. Ren, Z. L. He, H. Z. Zhao and T. Zhu, *Rare Met.*, 2022, **41**, 830–835.
- 38 C. Hu, P. Pan, H. Huang and H. Liu, *Biosensors*, 2022, **12**, 813.
- 39 R. M. Rego, G. Sriram, K. V. Ajeya, H. Y. Jung, M. D. Kurkuri and M. Kigga, *J. Hazard. Mater.*, 2021, **416**, 125941.
- 40 T. T. M. Bui, L. T. Nguyen, N. P. H. Pham, C. C. Tran, L. T. Nguyen, T. A. Nguyen, H. N. Nguyen and M. V. Nguyen, *RSC Adv.*, 2021, **11**, 36626–36635.
- 41 C. C. Tran, H. C. Dong, V. T. N. Truong, T. T. M. Bui, H. N. Nguyen, T. A. T. Nguyen, N. N. Dang and M. V. Nguyen, *Dalton Trans.*, 2022, **51**, 7503–7516.
- 42 Z. Hasan and S. H. Jhung, *J. Hazard. Mater.*, 2015, **283**, 329–339.
- 43 M. S. Khan, M. Khalid and M. Shahid, *Mater. Adv.*, 2020, **1**, 1575–1601.
- 44 D. K. Yoo, G. Lee, Md. M. H. Mondol, H. J. Lee, C. M. Kim and S. H. Jhung, *Coord. Chem. Rev.*, 2023, **474**, 214868.
- 45 H. Yang, F. Peng, A. N. Hong, Y. Wang, X. Bu and P. Feng, *J. Am. Chem. Soc.*, 2021, **143**, 14470–14474.
- 46 B. Wang, Y. Ma, W. Xu and K. Tang, *Langmuir*, 2022, **38**, 8954–8963.
- 47 N. Abdolrahimi and A. Tadjarodi, *Proceedings*, 2019, **41**, 51.
- 48 H. He, K. Chai, T. Wu, Z. Qiu, S. Wang and J. Hong, *Materials*, 2022, **15**, 4058.
- 49 F. Yang, G. Xu, Y. Dou, B. Wang, H. Zhang, H. Wu, W. Zhou, J. Li and B. Chen, *Nat. Energy*, 2017, **2**, 877–883.
- 50 A. Sonnauer, F. Hoffmann, M. Fröba, L. Kienle, V. Duppel, M. Thommes, C. Serre, G. Férey and N. Stock, *Angew. Chem.*, 2009, **121**, 3849–3852.
- 51 M. J. Uddin, R. E. Ampiaiw and W. Lee, *Chemosphere*, 2021, **284**, 131314.
- 52 I. Arbeloa and P. Ojeda, *Chem. Phys. Lett.*, 1981, **79**, 347–350.
- 53 H. Zhu, J. Wu, M. Fang, L. Tan, C. Chen, N. Alharbi, T. Hayat and X. Tan, *RSC Adv.*, 2017, **7**, 36231–36241.
- 54 Z. He, Y. Yang, P. Bai and X. Guo, *J. Ind. Eng. Chem.*, 2019, **77**, 262–272.
- 55 J. A. S. Costa, V. H. Sarmento, L. P. Romão and C. M. Paranhos, *Biomass Convers. Biorefin.*, 2020, **10**, 1105–1120.
- 56 C. X. Yu, K. Z. Wang, X. J. Li, D. Liu, L. F. Ma and L. L. Liu, *Cryst. Growth Des.*, 2020, **20**, 5251–5260.
- 57 H. Wang, D. B. Jiang, J. Gu, L. Ouyang, Y. X. Zhang and S. Yuan, *Ind. Eng. Chem. Res.*, 2020, **59**, 6065–6077.
- 58 J. Zhang, F. Li and Q. Sun, *Appl. Surf. Sci.*, 2018, **440**, 1219–1226.
- 59 H. Liu, X. Ren and L. Chen, *J. Ind. Eng. Chem.*, 2016, **34**, 278–285.
- 60 H. Tian, J. Peng, T. Lv, C. Sun and H. He, *J. Solid State Chem.*, 2018, **257**, 40–48.
- 61 B. Li, W. Jiang, Y. Xu, Z. Xu, Q. Yan and G. Yong, *Dyes Pigm.*, 2020, **174**, 108017.
- 62 L. Zeng, L. Xiao, Y. Long and X. Shi, *J. Colloid Interface Sci.*, 2018, **516**, 274–283.
- 63 H. Guo, F. Lin, J. Chen, F. Li and W. Weng, *Appl. Organomet. Chem.*, 2015, **29**, 12–19.
- 64 C. Yang, S. Wu, J. Cheng and Y. Chen, *J. Alloys Compd.*, 2016, **687**, 804–812.
- 65 G. Vijayakumar, R. Tamilarasan and M. Dharmendirakumar, *J. Mater. Environ. Sci.*, 2012, **3**, 157–170.

